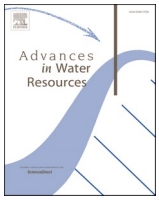
Advances in Water Resources 218 (2026) 105523



Contents lists available at ScienceDirect

Advances in Water Resources

journal homepage: www.elsevier.com/locate/advwatres



Structural heterogeneity regulates Rayleigh-Darcy convection in porous media at statistically steady state

Jingwei Zhu [a], Jingsen Feng [a], Chiyu Xie [b], Hang Deng [a,c,*], Jianing Yang [a], Yumin Wang [a,d], Ke Xu [a,c,*]

[a] Department of Energy and Resources Engineering, School of Mechanics and Engineering Science, Peking University, Beijing, 100871, PR China
[b] School of Astronautics, Beihang University, Beijing, 100191, PR China
[c] Institute of Energy, Peking University, Beijing, 100871, PR China
[d] School of Emergency Management and Safety Engineering, China University of Mining & Technology, Beijing, 100083, PR China

ARTICLE INFO

Keywords:
Convective solute transport
Structurally heterogeneous porous media
Preferential flow
Lattice Boltzmann method

ABSTRACT

Rayleigh-Darcy (R-D) convection in fluid-saturated porous media is triggered by buoyancy when concentration (or temperature) contrasts induce an unstable density stratification, characterized by denser fluid overlying less dense fluid. This phenomenon commonly occurs in geological carbon dioxide (CO_2) sequestration, permafrost thawing, and strata with high geothermal gradients. R-D convection in turn governs solute mixing dynamics, including transport patterns within porous media and transfer rates across boundaries. Despite extensive research on solute transport kinetics in homogeneous media, a significant gap persists in understanding the effect of the structural heterogeneity (here characterized by a preferential flow pathway). This gap is critical as heterogenous porous media are ubiquitous in subsurface hydrological formations and often exist dominant flow pathways. This paper investigates how a single vertical high-permeability channel regulates transport patterns and influences transfer rates in R-D convection at statistically steady state. Simulations with Rayleigh-Darcy number Ra_D ranging from 5.7×10^2 to 5.4×10^4 are performed using the Lattice Boltzmann Method (LBM), and the evolving transport patterns and transfer rates are recorded after systems reach statistically steady state. The most numerical simulations reveal a consistent transport pattern: denser fluid preferentially descends through the dominant channel, whereas the lighter fluid ascends mainly through the surrounding porous media. Compared with homogeneous media, the presence of the flow channeling enhances the solute transfer rate at lower Ra_D ($Ra_D < 1.3 \times 10^3$) while suppresses it at higher Ra_D ($Ra_D > 1.0 \times 10^4$). We propose that the transport pattern is determined by the minimization of total gravitational potential energy, and formulate a theoretical criterion that successfully predicts the patterns obtained from simulations. Comparative analysis of R-D convection characteristics across Ra_D in homogeneous versus structurally heterogeneous media, demonstrates that this contrasting influence of the high-permeability pathway on transfer rates results from the channel promoting a columnar flow pattern at lower Ra_D, whereas it induces a large-scale circulation at higher Ra_D. Moreover, the regulation role of the dominant channel is shown to suppress flow stochasticity when $Ra_D < 1.3 \times 10^3$ and $Ra_D > 7.0 \times 10^3$. The insights from the simple system first uncover the effect of a vertical high-permeability pathway on transport patterns and transfer rates in R-D convection at statistically steady state, providing a theoretical basis relevant to subsurface hydrological engineering including geo-energy resource extraction and storage.

1. Introduction

Rayleigh-Darcy convection arises from an unstable fluid configuration in porous media, where a denser fluid overlies a less dense fluid due to concentration (or temperature) contrasts (De Paoli, 2022). This buoyancy-driven convection governs solute (or thermal) mixing in a wide range of subsurface hydrological systems (Anderson and Guba, 2020; De Paoli et al., 2023), Relevant phenomena include the evolution of salt polygons via near-surface evaporation and groundwater flow in arid regions (Lasser et al., 2023), water and solute redistribution

* Corresponding authors at: Department of Energy and Resources Engineering, School of Mechanics and Engineering Science, Peking University, Beijing 100871, PR China.
E-mail addresses: hangdeng@pku.edu.cn (H. Deng), kexu1989@pku.edu.cn (K. Xu).

https://doi.org/10.1016/j.advwatres.2026.105523
Received 8 September 2026; Received in revised form 4 October 2026; Accepted 4 October 2026
Available online 6 October 2026
0309-1708/© 2026 Elsevier Ltd. All rights are reserved, including those for text and data mining, AI training, and similar technologies.

during permafrost thaw (Wang et al., 2025), and fluid circulations in supercritical geothermal systems (Parisio et al., 2019). Furthermore, geological carbon dioxide sequestration, a promising technology to mitigate atmospheric greenhouse gas levels (Huppert and Neufeld, 2014; Teng et al., 2020), makes R-D convection a research hotspot in recent years (Li et al., 2025). During sequestration, injected CO_2 migrates upward within saline aquifers due to its buoyancy, accumulates beneath low-permeability caprocks, and gradually dissolves into the underlying brine (Zhao et al., 2014). The resulting CO_2-enriched brine is generally denser than the ambient fluid, triggering R-D convection that transports dissolved CO_2 deeper into the formation (Iding and Blunt, 2011). This convective mixing enhances storage efficiency and security, as aqueous CO_2 may undergo mineralization reactions that permanently sequester it in the subsurface (Sun et al., 2023). Therefore, a thorough understanding of solute transport dynamics in R-D convection, including solute transport patterns within porous strata and solute transfer rates across fluid-fluid interfaces, is crucial for assessing storage efficiency, preventing leakage, and ensuring long-term sequestration integrity (Dutta et al., 2025; Li et al., 2025).

Extensive research, including rigorous theoretical derivations (Horton and Rogers, 1945; Hewitt et al., 2013; Letelier et al., 2019), advanced experiments (De Paoli et al., 2020; Wang et al., 2021; Liyanage et al., 2024), high-resolution numerical simulations (Hidalgo and Carrera, 2009; Slim, 2014; Sabet et al., 2021; Ju et al., 2022), and new applications of artificial intelligence techniques (Talabi et al., 2026), has elucidated transport patterns and transfer rates across different temporal stages in homogeneous porous media. However, subsurface formations commonly exhibit structural heterogeneity (here characterized by a vertically dominant channel; as shown in Fig. 1**a**), as evidenced by numerous field studies (Iding and Ringrose, 2010; Bond et al., 2017; Han et al., 2024). Consequently, R-D convection in heterogeneous (or fractured) media has attracted growing research interest (Hosseini et al., 2020; Liu and Yao, 2023; Xuan et al., 2024; Zhang et al., 2024) across diverse aspects such as the onset of the convection (Kaydani and Mohebbi, 2017) and the anisotropy effect (De Paoli et al., 2016; Li et al., 2020). Early studies show that a dominant channel preferentially transports dense plumes (Graf and Therrien, 2005), with solute transfer rates increasing with Rayleigh number (Chen and Zhang, 2010). In contrast, other works reported the role of preferential channels, as pathways for denser fluid or for fresh water, varies temporally (Kim et al., 2019), and the presence of high-permeability pathways can either enhance or suppress solute transfer rates relative to homogeneous media (Vujević et al., 2014). Overall, while it is established that high-permeability pathways affect both solute transport patterns (acting as preferential pathway for denser fluid or lighter fluid) (Yang et al., 1998) and transfer rates (increasing or decreasing solute transfer rates compared with homogeneous porous media) in R-D convection (Murphy, 1979; Mezon et al., 2018; Xu et al., 2024), a consistent mechanistic understanding remains elusive. Crucially, whether for natural processes evolving over annual timescales (e.g., salt polygon formation in arid regions) or engineering applications operating across decadal horizons (e.g., geothermal extraction), the system behavior is ultimately governed by its statistically steady state (Hewitt, 2020). Hence, analyzing R-D convection under steady-state conditions is essential for reliably predicting long-term performance. However, despite its importance, a comprehensive theoretical framework capable of explaining the statistically steady-state transport patterns and solute transfer rates in structurally heterogeneous porous media is still lacking.

In this study, we adopt a pore-scale perspective to investigate R-D convection in structurally heterogeneous porous media, as hydrodynamic dispersion fundamentally affects convective transport (Tsinober et al., 2023) yet its coefficient remains challenging to accurately quantify at the Darcy scale (Shikaze et al., 1998; Landman et al., 2007; Nick et al., 2009). Specifically, we employ the Lattice Boltzmann Method (LBM) with coupled double-distribution LBGK models. Using a Rayleigh–Bénard (RB) configuration (Benhammadi and Hidalgo, 2025) (Fig. 1**b**), we focus on statistically steady-state solute transport patterns and transfer rates. A theoretical model is developed to rationalize why distinct transport patterns emerge. Furthermore, we clarify the underlying mechanism responsible for a dominant channel in either enhancing or suppressing solute transfer rates.

2. Pore-scale modeling

2.1. Problem setup

As illustrated by Fig. 1**b**, a two-dimensional fluid-saturated heterogeneous porous medium with a vertically preferential channel embedded in the background porous medium is considered. The origin of the coordinates system is located at the top of the domain, with X axis pointing downward along the direction of gravity $\vec{g}^*$ and Y axis pointing rightward along the horizontal direction. Dirichlet boundary conditions for the concentration, $C^*_{top} \equiv C^*_{max}$ and $C^*_{bottom} \equiv C^*_{min}$, are imposed on the top and bottom boundary, respectively, and the fluid density ρ^* is assumed to depend linearly on the concentration

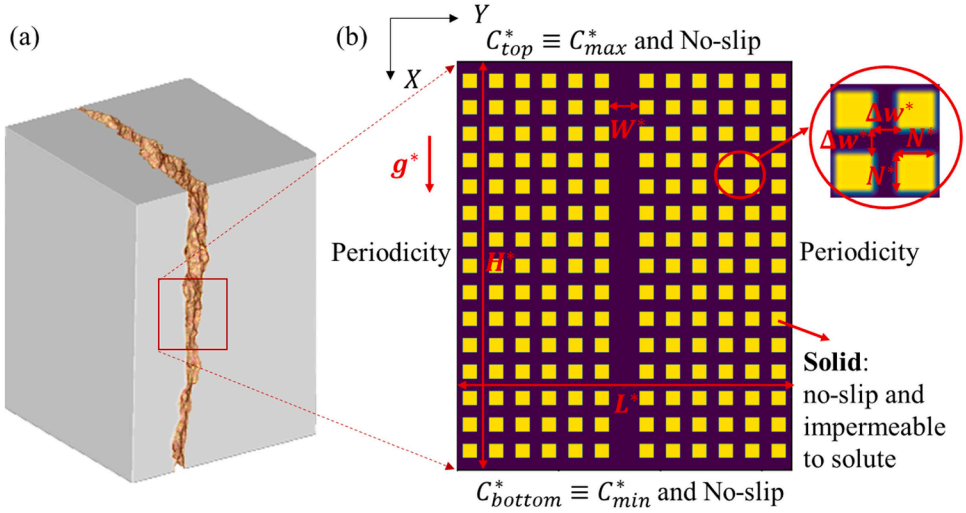


Fig. 1. Problem setup for investigating R-D convection at statistically steady state: (a) a digital rock image of a structurally heterogeneous medium (Santos et al., 2021); (b) sketch of computational domain: a rectangle of size $L^* \times H^*$ containing a preferential channel of width W^*, a surrounding porous medium with pore size Δw^*, and square solid particles of side length N^*.

$$\rho^*(C^*) = \rho^*_{ref}\left[1+\beta^*\left(C^* - C^*_{ref}\right)\right] \tag{1}$$

where $C^*_{ref} = (C^*_{max} - C^*_{min})/2$ is the reference concentration, ρ^*_{ref} denotes reference fluid density, and β^* represents the coefficient of the effect of concentration on fluid density. The superscript * indicates physical variables. The validity of the Boussinesq approximation is also assumed, then the flow is incompressible and controlled by the continuity equation and Navier-Stokes equation

$$\vec{\nabla}\cdot\vec{u}^* = 0 \tag{2}$$

$$\frac{\partial \vec{u}^*}{\partial t^*} + \vec{u}^*\cdot\vec{\nabla}\vec{u}^* = \frac{1}{\rho^*}\vec{\nabla}p^* + \nu^*\nabla^2\vec{u}^* + \vec{g}^*\beta^*\left(C^* - C^*_{ref}\right) \tag{3}$$

where $\vec{u}^*$ represents velocity field, p^* is pressure, and ν^* and t^* denote kinematic viscosity and time, respectively. The top and bottom boundaries are no-slip for fluid flow.

The evolution of concentration field is governed by the advection-diffusion equation

$$\frac{\partial C^*}{\partial t^*} + \vec{\nabla}\cdot\left(\vec{u}^* C^*\right) = \vec{\nabla}\cdot\left(D^*\vec{\nabla}C^*\right) \tag{4}$$

where D^* is the diffusion coefficient. For the lateral boundaries, periodicity is considered for both flow and concentration fields. The fluid-solid interface is no-slip and impermeable to the solute. At the initial time, $\vec{u}^* = 0$ and the vertically linear distribution of the concentration from C^*_{min} to C^*_{max} are adopted. We verify that the initial conditions have a negligible influence on the R-D convection at statistically steady state as shown in Appendix A, and Hu et al. (2023) also proves that the initial concentration distribution do not affect the ultimate regime of R-D convection.

In this setup, there are two dimensionless parameters controlling the system including Rayleigh-Darcy number $Ra_D = \frac{g^*\beta^*\left(C^*_{max}-C^*_{min}\right)H^*k^*_{vet}}{\varnothing D^*\nu^*}$ (measuring the ratio of the characteristic time scale for diffusion to that for convection) and Schmidt number $Sc = \frac{\nu^*}{D^*}$ (representing the ratio of momentum diffusivity to solute diffusivity). Furthermore, the corresponding dimensionless response parameter is Sherwood number $Sh = \frac{\left\langle \frac{\partial C^*}{\partial X^*}\right\rangle_{X^*=0}}{\left(C^*_{max}-C^*_{min}\right)H^{*-1}}$ (a dimensionless measure of the solute transfer rate that quantifies the ratio of the total solute flux to the diffusive solute flux). Here, the bracket $\langle\cdot\rangle_{X^*=x^*}$ represents the average over a horizontal plane at $X^* = x^*$, H^* are the height of the simulation domain, $\varnothing$ denotes porosity, and k^*_{vet} is the permeability of porous media along the vertical direction. The detailed calculation process for permeability k^*_{vet} (as well as the vertical permeabilities of the preferential channel and surrounding porous medium, k^*_{ch} and k^*_m) in porous media is illustrated in Appendix B. Without loss of generality, we focus our attention to the cases of $Sc = 500$ with concentration not affecting the fluid viscosity (Hidalgo et al., 2012; Zhu et al., 2024). A comprehensive list of all assumptions adopted in this study is provided in Table C of the Appendix C.

2.2. Computational details

The numerical simulations are performed using LBM. To convert the physical quantities from physical unit (with superscript *) to the lattice unit (without superscript *), three basic lattice quantities, viscosity $\nu = \frac{1}{3.1}$, reference density $\rho_{ref} = 1$, and spatial resolutions in both X and Y directions $\Delta x = \Delta y = 1$ are set. Here, the value of lattice viscosity is chosen to ensure numerical stability (Wang and Pan, 2008). Furthermore, the concentration is normalized through $C = \frac{C^*-C^*_{min}}{C^*_{max}-C^*_{min}}$, therefore, $C_{max} = 1$, $C_{min} = 0$, $\Delta C = 1$, and $C_{ref} = 0.5$. Table 1 lists the corresponding values of the physical quantities in the physics-based and lattice-based systems, and the detailed derivations for all conversion coefficients are shown in Appendix D.

Here, the D2Q9 (two dimensions and nine discrete velocity directions) model and the D2Q5 (two dimensions and five discrete velocity directions) model are chosen to simulate the fluid flow and solute transport, respectively, which is based on the coupled LBGK equations (Krüger et al., 2017)

$$f_i\left(\vec{x}+\vec{e}_i\Delta t, t+\Delta t\right) = f_i(\vec{x},t) + \frac{\Delta t}{\tau_f}\left(f_i(\vec{x},t) - f_i^{eq}(\rho,\vec{x})\right) + \Delta t F_i \tag{5}$$

$$s_i\left(\vec{x}+\vec{e}_i\Delta t, t+\Delta t\right) = s_i(\vec{x},t) + \frac{\Delta t}{\tau_s}\left(s_i(\vec{x},t) - s_i^{eq}(C,\vec{x})\right) \tag{6}$$

where $f_i(\vec{x},t)$ $(i = 0,1,\ldots,8)$ and $s_i(\vec{x},t)$ $(i = 0,1,\ldots,4)$ are the particle distribution functions for fluid flow and solute transport, respectively, which represent the number of fluid and solute particles at lattice position $\vec{x}$ and lattice time t traveling along the i^{th} direction; Δt is time interval, which is set to be 1;

$$\vec{e}_i = \begin{cases} (0,0) & i = 0 \\ \left(cos\left[(i-1)\frac{\pi}{2}\right], sin\left[(i-1)\frac{\pi}{2}\right]\right) & i = 1,2,3,4 \\ \left(\sqrt{2}cos\left[(2i-1)\frac{\pi}{4}\right], \sqrt{2}sin\left[(2i-1)\frac{\pi}{4}\right]\right) & i = 5,6,7,8 \end{cases}$$

and $F_i = \left(1-\frac{\Delta t}{2\tau_f}\right)\frac{f_i^{eq}}{\rho}\frac{\vec{e}_i-\vec{u}}{c_s^2}\cdot\vec{F}$ (He et al., 1998) denotes the discrete velocity directions and force corresponding to direction i, respectively, in which $c_s = \frac{1}{\sqrt{3}}$, $\vec{u}$, and $\vec{F} = \rho_{ref}\vec{g}\beta(C-C_{ref})$ mean lattice sound speed, velocity, and buoyancy force, respectively; $\tau_f = \frac{3\nu\Delta t}{(\Delta x)^2} + 0.5$ and $\tau_s = \frac{3D\Delta t}{(\Delta x)^2} + 0.5$ represent relaxation time related to the kinematic viscosity ν and diffusion coefficient D; and $f_i^{eq}(\rho,\vec{u}) = \rho\omega_i^f\left[1+\frac{\vec{e}_i\cdot\vec{u}}{c_s^2}+\frac{\left(\vec{e}_i\cdot\vec{u}\right)^2}{2c_s^4}-\frac{u^2}{2c_s^2}\right]$ and $s_i^{eq}(C,\vec{u}) = C\omega_i^s\left(1+\frac{\vec{e}_i\cdot\vec{u}}{c_s^2}\right)$ denote equilibrium distribution functions for fluid flow and solute transport at lattice position $\vec{x}$ and lattice time t traveling along the i^{th} direction, respectively, with $\omega_i^f = \begin{cases} \frac{4}{9} & i = 0 \\ \frac{1}{9} & i = 1,2,3,4 \\ \frac{1}{36} & i = 5,6,7,8 \end{cases}$ and $\omega_i^s = \begin{cases} \frac{1}{3} & i = 0 \\ \frac{1}{6} & i = 1,2,3,4 \end{cases}$. The macroscopic governing Eqs. 2–4 can be recovered through Chapman-Enskog analysis (Chen and Doolen, 1998) and the macroscopic quantities can be obtained by

$$\rho(\vec{x},t) = \sum_{i=0}^{8} f_i(\vec{x},t) \tag{7}$$

Table 1
Correspondence between physical and lattice units.

Physical quantity	Lattice symbol	Lattice value	Physical value
Spatial resolution	Δx, Δy	1	$25\mu m$
Reference density	ρ_{ref}	1	$10^3 kg/m^3$
Viscosity	ν	1/3.1	$10^{-6}m^2/s$
Time	t	1	$2\times10^{-4}s$
Gravity	g	1.593×10^{-2}	$9.8\ m/s^2$
Velocity	u	1	$0.124m/s$
Pressure	p	1	$15.376Pa$
Permeability	k	1	$6.25\times10^{-10}m^2$
Reference concentration	C_{ref}	0.5	$(C^*_{max} - C^*_{min})/2$

$$\vec{u}(\vec{x},t)=\frac{1}{\rho(\vec{x},t)}\sum_{i=0}^{8}f_i(\vec{x},t)\vec{e}_i+\frac{\vec{F}\Delta t}{2\rho(\vec{x},t)} \tag{8}$$

$$C(\vec{x},t)=\sum_{i=0}^{4}s_i(\vec{x},t) \tag{9}$$

The boundary conditions, no-slip, constant concentration, and solid impermeable to concentration, are implemented through back-bound, Zou-He, and no-flux boundary schemes, and the established model is fully validated with benchmarks as shown in Appendix E.

Table 2 summaries the details of simulation setups. Here, we first design 8 numerical cases (S1 ~ S8) with varying Ra_D values using the structurally heterogeneous porous medium shown in Fig. 1**(b)**. For comparison, we also construct the homogenous porous media (S9 ~ S16; $W = \Delta w$) with the similar geometry and corresponding Ra_D values. Furthermore, to examine the effect of larger values of $\frac{W}{\Delta w}$, we establish the cases S17 ~ S20. Finally, other 3 cases (S21 ~ S23) are developed to investigate the transport behavior when the preferential pathway is only slightly wider than the pore size of the surrounding porous medium.

2.3. Simulation results

Here, we show representative simulation results. Firstly, the rate of change of mean squared concentration $\frac{d[\![C^2]\!]}{dt}$ ($[\![\cdot]\!]$ denotes the average over the whole computational domain), as suggested by De Paoli (2023) and Hidalgo et al. (2012), is adopted to evaluate whether R-D convection reaches the steady state. Once the system attains a statistically steady state, the value of $\frac{d[\![C^2]\!]}{dt}$ slightly fluctuates around 0 as the solute flux through wall $F_{X=0}=\frac{\left\langle \frac{\partial C}{\partial \hat{x}} \right\rangle_{X=0}}{H}$ (external contribution; here the $\langle\cdot\rangle_{X=x}$ is the dimensionless counterpart of $\langle\cdot\rangle_{X^*=x^*}$) and the mean concentration dissipation $\chi = D[\![|\nabla C|^2]\!]$ (internal dissipation) reach statistical equilibrium (De Paoli, 2023). Fig. 2**(a)** shows the values of $\frac{d[\![C^2]\!]}{dt}$ and concentration evolutions for the typical case S5 at different time. At early stage, denser fluid goes downward through the dominant pathway, and the values of $\frac{d[\![C^2]\!]}{dt}$ start to deviate from 0. With time advancing, $\frac{d[\![C^2]\!]}{dt}$ reaches the minimum values and then increases until the result is around 0. It is worth mentioning that the fluctuations of $\frac{d[\![C^2]\!]}{dt}$ are relatively large before about 4 million time steps, therefore, 4 millionth time step is chosen as the starting point of the statistically steady state for the typical case.

In the later stage, the concentration distribution shows that the lighter fluid (shown in the bluer shades) mainly occupies the surrounding porous medium while denser fluid (shown in the redder shades) primarily concentrates near the high-permeability channel, which implies the transport pattern of R-D convection at statistically steady state for this typical case: the dominant channel mainly serving as the flow pathway for denser fluid whereas the surrounding porous medium primarily acting as routes for lighter fluid. To prove that, the average streamline field of all time at statistically steady state is plotted in Fig. 2**(b)**. The streamline field presents higher flow velocity around the preferential pathway and lower velocity in the surrounding porous medium. More importantly, the fluid flow direction in the preferential channel is downward and that in the porous medium is upward. This illustrates that for this case, after the R-D convection reaches the statistically steady state, denser fluid migrates downward through the dominant pathway as the top boundary is always C^*_{max} ($C = 1$) and the bottom boundary is always C^*_{min} ($C = 0$). Therefore, the preferential pathway regulates the transport pattern of R-D convection in this structurally heterogeneous porous medium. It is worth mentioning that the flow field exhibits asymmetry because the system enters a chaotic regime (Otero et al., 2004). Under such regime, spontaneous symmetry breaking occurs due to boundary-layer instability, leading to asymmetric flow and concentration fields (Hewitt., 2020).

Seven more cases (S1 ~ S4 and S6 ~ S8) with Ra_D ranging from 5.7×10^2 to 3.1×10^4 are simulated, and the net vertical velocity in the dominant channel $\vec{u}_{xc}=\frac{\int\int_{channel}\vec{u}_x dxdy}{\int\int_{channel}dxdy}$ of the average flow field of all time steps at statistically steady state is calculated. We further nondimensionalize $\vec{u}_{xc}$ by $Pe=\frac{u_{xc}H}{D}$ and define new dimensionless number $\frac{Pe}{Sh}$ representing the ratio of solute transfer flux in the preferential pathway over the total solute flux. Here, since the sign of u_{xc} demonstrates the flow direction, the resulting dimensionless number $\frac{Pe}{Sh}$ also

Table 2
Summary of simulations. Columns from left to right are simulation index, length and height of computational domain, the width of the preferential channel, the pore size of the surrounding porous medium, number of solid grids, the permeability of the porous medium in the vertical direction, the permeability of the preferential channel, the permeability of the surrounding porous medium, total porosity, the porosity of the surrounding porous medium, and Reyleigh-Darcy number.

Simulation	$L \times H$	W	Δw	N	k_{vet}	k_{ch}	k_m	$\varnothing$	$\varnothing_m$	Ra_D
S1	320 × 402	20	12	14	9.0	31.3	7.3	72.6%	67.0%	5.7×10^2
S2	320 × 402	20	12	14	9.0	31.3	7.3	72.6%	67.0%	7.7×10^2
S3	320 × 402	20	12	14	9.0	31.3	7.3	72.6%	67.0%	1.5×10^3
S4	320 × 402	20	12	14	9.0	31.3	7.3	72.6%	67.0%	3.8×10^3
S5	320 × 402	20	12	14	9.0	31.3	7.3	72.6%	67.0%	7.7×10^3
S6	320 × 402	20	12	14	9.0	31.3	7.3	72.6%	67.0%	1.5×10^4
S7	320 × 402	20	12	14	9.0	31.3	7.3	72.6%	67.0%	2.3×10^4
S8	320 × 402	20	12	14	9.0	31.3	7.3	72.6%	67.0%	3.1×10^4
S9	312 × 402	12	12	14	7.3	\	7.3	67.0%	67.0%	5.7×10^2
S10	312 × 402	12	12	14	7.3	\	7.3	67.0%	67.0%	7.7×10^2
S11	312 × 402	12	12	14	7.3	\	7.3	67.0%	67.0%	1.5×10^3
S12	312 × 402	12	12	14	7.3	\	7.3	67.0%	67.0%	3.9×10^3
S13	312 × 402	12	12	14	7.3	\	7.3	67.0%	67.0%	7.7×10^3
S14	312 × 402	12	12	14	7.3	\	7.3	67.0%	67.0%	1.5×10^4
S15	312 × 402	12	12	14	7.3	\	7.3	67.0%	67.0%	2.3×10^4
S16	312 × 402	12	12	14	7.3	\	7.3	67.0%	67.0%	3.1×10^4
S17	288 × 402	40	12	14	25.9	126.8	7.3	74.6%	67.0%	2.1×10^4
S18	288 × 402	40	12	14	25.9	126.8	7.3	74.6%	67.0%	5.4×10^4
S19	308 × 402	60	12	14	67.0	287.6	7.3	76.3%	67.0%	2.7×10^4
S20	308 × 402	60	12	14	67.0	287.6	7.3	76.3%	67.0%	5.4×10^4
S21	309 × 404	13	12	2	11.36	10.7	11.2	98.0%	97.7%	7.2×10^3
S22	309 × 404	13	12	2	11.36	10.7	11.2	98.0%	97.7%	1.4×10^4
S23	309 × 404	13	12	2	11.36	10.7	11.2	98.0%	97.7%	3.6×10^4

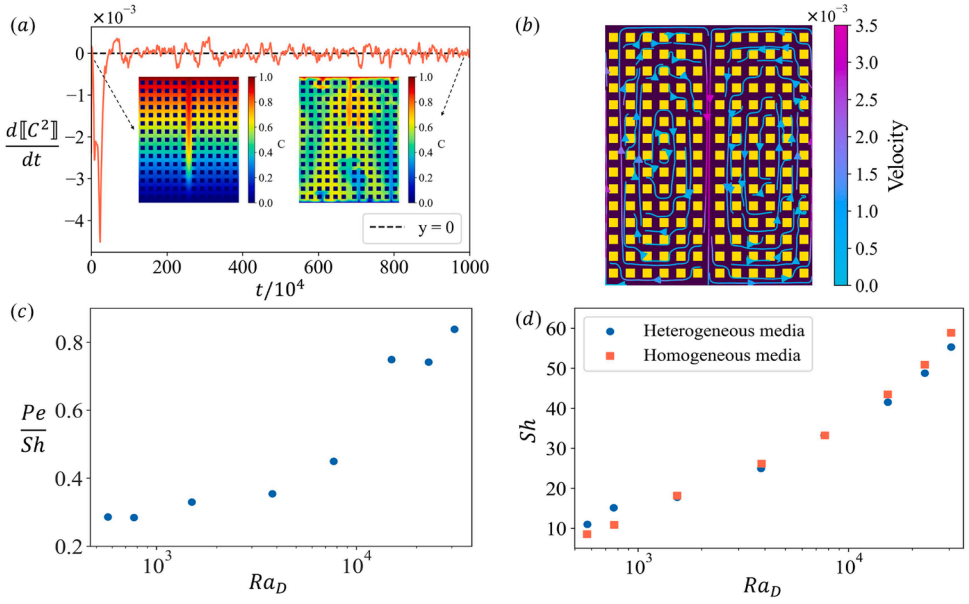


Fig. 2. Simulation results: (a) the rate of change of mean squared concentration $\frac{d[\![C^2]\!]}{dt}$ and the concentration field for case S5 at different time; (b) the average streamline field of all time at statistically steady state of case S5; (c) the relationship between $\frac{Pe}{Sh}$ and Ra_D for the structurally heterogeneous porous medium (S1 ~ S8); (d) the relationship between Sh and Ra_D for both the structurally heterogeneous porous medium (S1 ~ S8) and the homogeneous medium (S9 ~ S16).

carries a sign, which reflects the direction of fluid flow within the dominant channel.

Fig. 2**(c)** reveals that $\frac{Pe}{Sh}$, plotted against Ra_D, is always greater than 0. This represents a universal transport pattern for all investigated Ra_D: denser fluid primarily descends through the preferential pathway while lighter fluid mainly ascends through the surrounding porous medium. Furthermore, the values of $\frac{Pe}{Sh}$ generally increase with the Ra_D, ranging from 0.29 to 0.81, which indicates that an increase in Ra_D enhances the solute transfer flux within the dominant channel.

Given that the preferential channel regulates the transport pattern in R-D convection at statistically steady state, it naturally follows to consider whether it also affects the solute transfer rate. Therefore, the corresponding cases of the homogeneous porous medium with different Ra_D are simulated (S9 ~ S16).

Fig. 2**(d)** compares the resulting Sh values for the structurally heterogeneous and homogeneous media at different Ra_D. Surprisingly, Sh in the heterogeneous medium is larger than that in the homogeneous medium when the Ra_D is relatively low (lower than around 1.3×10^3), however, Sh in the heterogeneous medium is smaller than that in the homogeneous medium when the Ra_D is relatively high (higher than around 1×10^4). Thus, the presence of the dominant channel can increase or decrease the rate depending on Ra_D. This is consistent with Kim et al. (2019). It is worth mentioning that $Ra_D = 1.3 \times 10^3$ serves as a critical threshold not only for the relative magnitude of the Sh between the structurally heterogeneous and homogeneous media, but also for the transition in flow regimes of R-D convection (Otero et al., 2004). Therefore, for different flow regimes, the influence of the preferential pathway on the solute transfer rate is different.

In summary, there are two key findings for R-D convection at statistically steady state:

1) the high-permeability pathway regulates the solute transport pattern, which is independent of Ra_D;
2) the high-permeability pathway influences the relative magnitude of Sh between the structurally heterogeneous and homogeneous media, which depends on Ra_D.

3. A theoretical model for transport patterns

Although the regulation effect of the preferential pathway on the solute transport pattern in R-D convection at statistically steady state is observed, the underlying physical mechanism remains unclear. Inspired by the GL theory (Grossmann and Lohse, 2000, 2001), we recognize that in R-D convection, the viscous shear dissipates the buoyancy-driven kinetic energy that originates from an unstable concentration distribution (resulting the denser fluid on the top while the lighter fluid on the bottom). The unstable concentration distribution essentially leads to relatively higher gravitational potential energy of its system compared with that of the stable concentration distribution system (resulting the lighter fluid on the top whereas the denser fluid on the bottom). To reduce the gravitational potential energy of a system with an unstable concentration distribution, the convection emerges, which leads to the energy conversion from the gravitational potential energy to the kinetic energy.

Therefore, starting from the energy perspective, we calculate the total gravitational potential energy $E_{gp} = \int\int \rho g(H-x)\, dxdy$ (the reference plane being the bottom of whole computational domain; both the positive x-axis and gravity g pointing vertically downwards as shown in Fig. 1) and the total kinetic energy $E_{ki} = \int\int \frac{1}{2}\rho|\vec{u}|^2\, dxdy$ of the system for each time. Across all cases, E_{gp} is consistently much higher than E_{ki}, as evidenced in Appendix F. This is because the gravitational potential energy associated with an unstable concentration distribution is only partially converted to the kinetic energy. Thus, we neglect the total kinetic energy and hypothesize that the minimization of total gravitational potential energy dominates the transport pattern in R-D convections at statistically steady state.

To validate the hypothesis, we conceptually divide a statistically steady-state R-D convection pattern into two complementary subdomains (subdomain 1 with area A_1 and subdomain 2 with area A_2) with opposite vertical flow directions, as shown in Fig. 3**(a)**. One subdomain contains the downward plumes (associated with denser fluid and redder shades), while the other contains the upward plumes (associated with lighter fluid and bluer shades), and their flow directions will be determined by the subsequent derivation. Here, the very small area of possible transitional zones where the fluid's vertical velocity component

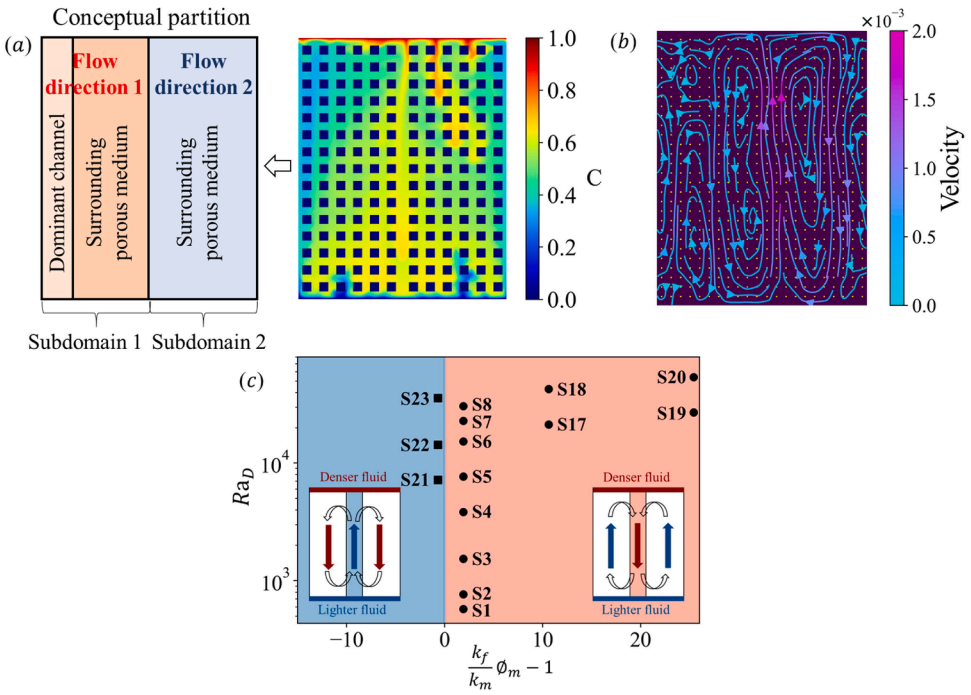


Fig. 3. (a) the schematic diagram of the theoretical model; (b) the average streamline field of all time at statistically steady state of case S21; (c) the phase diagram for verifying theoretical criterion with all structurally heterogeneous cases.

vanishes is neglected. As evidenced by the typical cases (S1 ~ S8) in Fig. 2**(b)** and Fig. 2**(c)**, the fluid within the dominant channel exhibits the unidirectional flow in a statistically steady state. Therefore, we assume unidirectional flow within the preferential channel in the conceptual model. Since the high-permeability channel (with area A_c) must belong to one of the two subdomains, it can be assigned to subdomain 1 without loss of generality. Furthermore, as density variations are small under the Boussinesq approximation and further reduce within each subdomain, the fluid density is assumed to be uniform within each subdomain, denoted by ρ_1 and ρ_2, respectively. Therefore, the total gravitational potential energy of the system can be written as $E_{gp} = \frac{1}{2}gH(\rho_1 A_1 \varnothing_1 + \rho_2 A_2 \varnothing_2)$ with $\varnothing_1$ and $\varnothing_2$ being the porosity in subdomain 1 and subdomain 2, respectively. Thus, the objective is to minimize $\rho_1 A_1 \varnothing_1 + \rho_2 A_2 \varnothing_2$. It should be noted that $\varnothing_2$ is approximated as the porosity of surrounding porous medium $\varnothing_m$ as the high-permeability channel is included in subdomain 1. Furthermore, the same viscosity is adopted for both subdomains because of concentration not affecting fluid viscosity. The all assumptions used here are listed in Table C of the Appendix C.

Next, theoretical derivations are conducted to establish a toy criterion for the prediction of the transport pattern in R-D convection at statistically steady state in structurally heterogeneous porous media. According to Darcy's law,

$$\frac{u_1}{u_2} = \frac{\frac{k_1}{\mu}\Delta\rho g}{\frac{k_2}{\mu}\Delta\rho g} = \frac{k_1}{k_2} \tag{10}$$

where u_1 and u_2 are the vertical Darcy velocities of plumes in the subdomain 1 and 2, respectively, k_1 and $k_2 = k_m$ represent the vertical permeabilities of the subdomain 1 and 2, respectively, with k_m being the vertical permeability of the surrounding porous medium, μ denotes the dynamic viscosity, and $\Delta\rho = |\rho_1 - \rho_2|$ is the fluid density difference. Since the subdomain 1 consists of the dominant channel and a part of the surrounding porous medium (with area A_{m1}) connected in parallel along the vertical direction,

$$k_1 = \frac{A_c k_{ch} + A_{m1} k_m}{A_1} = \frac{A_c k_{ch} + (A_1 - A_c)k_m}{A_1} \tag{11}$$

according to effective permeability theory (Peters, 2012), where k_{ch} denotes the vertical permeability of the dominant channel. In terms of Darcy-scale fluid continuity, the equation $\frac{A_2}{A_1} = \frac{u_1}{u_2}$ is obtained. Therefore,

$$\frac{A_2}{A_1} = \frac{A_c k_{ch} + (A_1 - A_c)k_m}{A_1 k_m} \tag{12}$$

Based on porosity definition and the geometry relationship,

$$\varnothing_1 = \frac{A_c + (A_1 - A_c)\varnothing_m}{A_1} \tag{13}$$

Thus,

$$\begin{aligned} A_2\varnothing_2 - A_1\varnothing_1 &= \frac{A_c k_{ch} + (A_1 - A_c)k_m}{k_m}\varnothing_m - A_c - (A_1 - A_c)\varnothing_m \\ &= \left(\frac{k_{ch}}{k_m}\varnothing_m - 1\right)A_c \end{aligned} \tag{14}$$

The Eq. (14) gives the theoretical criterion $\frac{k_{ch}}{k_m}\varnothing_m - 1$ for the prediction of the transport pattern in R-D convection at statistically steady state in structurally heterogeneous porous media. When $\frac{k_{ch}}{k_m}\varnothing_m - 1 > 0$, we have $A_2\varnothing_2 > A_1\varnothing_1$. Therefore, $\rho_2 < \rho_1$ as $\rho_1 A_1 \varnothing_1 + \rho_2 A_2 \varnothing_2$ tends to be minimal according to rearrangement inequality (Day, 1972). The $\rho_2 < \rho_1$ means that denser fluid descends in the subdomain 1 and lighter fluid ascends in the subdomain 2, which further illustrates denser fluid descends through the dominant channel and lighter fluid ascends through the surrounding porous medium because $A_c \in A_1$ the dominant channel is included in the subdomain 1. Similarly, when $\frac{k_{ch}}{k_m}\varnothing_m - 1 < 0$, we have $\rho_2 > \rho_1$, which means denser fluid migrates downward through the surrounding porous medium and lighter fluid goes upward through the dominant channel.

Finally, the theoretical criterion is verified with simulation results. For the structure of the case S5, the value of $\frac{k_{ch}}{k_m}\varnothing_m - 1$ is larger than 0 (detailed values of the physical quantities are summarized in Table 2), therefore, the denser fluid migrates downward through the dominant channel, which is

consistent with the simulation results. It is worth mentioning that the criterion is independent of Ra_D and only the function of structure information of the structurally heterogeneous porous media. This is also in good agreements with the finding in Section 2.3. To further prove the generality of the scenario $\frac{k_{ch}}{k_m}\varnothing_m - 1 > 0$, the other four cases, S17 ~ S20 (involving two distinct configurations with each having two different Ra_D), are simulated, and all simulation results agree well with the theoretical predictions.

For the scenario $\frac{k_{ch}}{k_m}\varnothing_m - 1 < 0$, this is not common under subsurface geological conditions as k_{ch} is usually much larger than k_m. To validate the theoretical criterion, we design the special structurally heterogeneous porous medium ($W = 13$ is slightly larger than the pore size of the surrounding porous medium $\Delta w = 12$), S21 ~ S23 (the same configuration with 3 different Ra_D), that satisfies $\frac{k_{ch}}{k_m}\varnothing_m - 1 < 0$. The average streamline field of all time at statistically steady state of case S21 is shown in Fig. 3**(b)**, which demonstrates the lighter fluid ascends through the dominant channel and denser fluid descends through the surrounding porous medium. This is in good agreements with the theoretical prediction. Moreover, the results of cases S22 and S23 show the same conclusion. Thus, the theoretical criterion is fully validated with simulations.

Fig. 3**(c)** shows the final phase diagram for the prediction of the transport pattern in R-D convection at statistically steady state. Consequently, the minimization of total gravitational potential energy is identified as the dominant mechanism governing the transport pattern in statistically steady-state R-D convection.

4. Analysis of solute transfer rates

Since the high-permeability pathway regulates the solute transport pattern in R-D convection at statistically steady state, it naturally follows

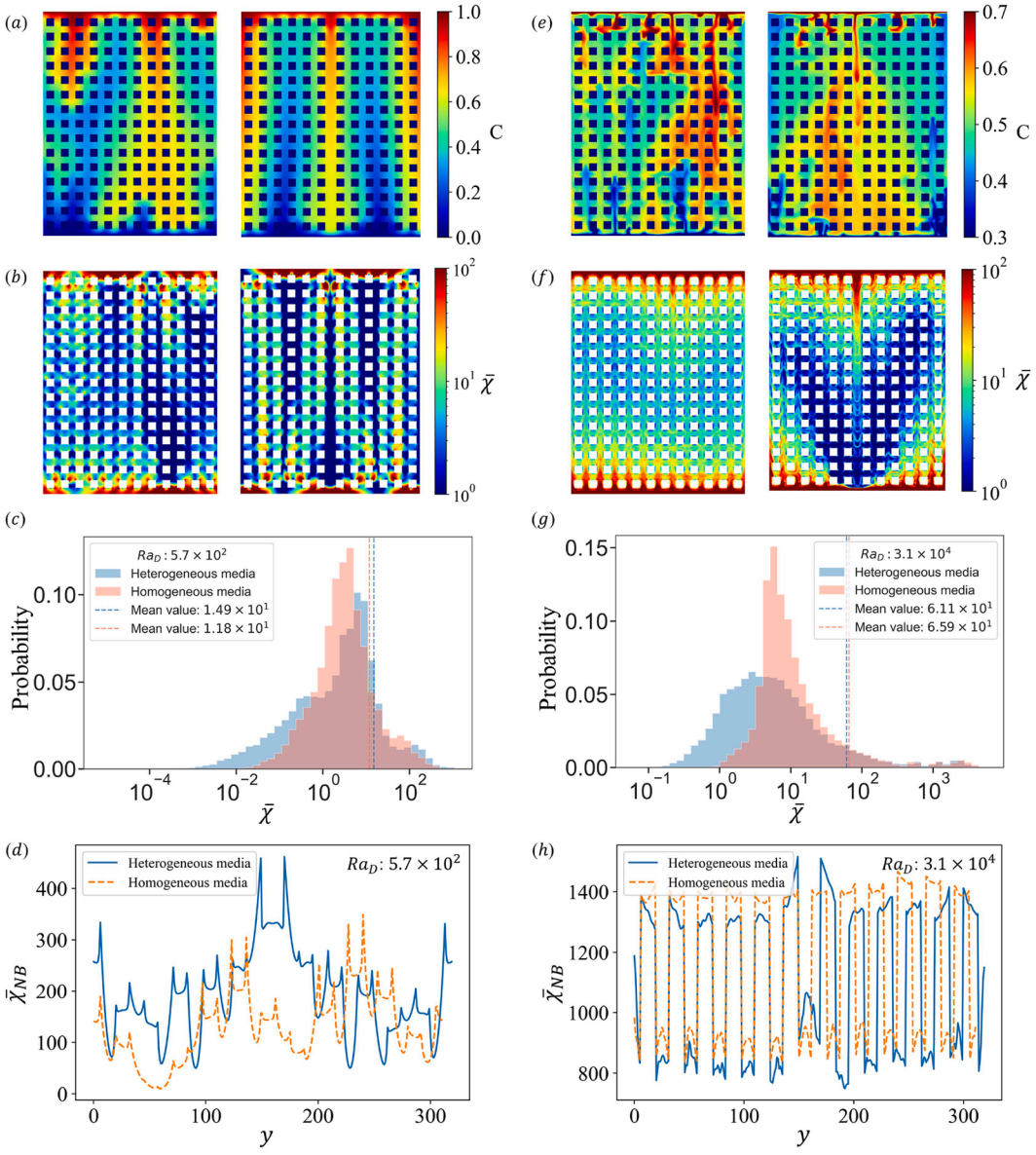


Fig. 4. (a) the instantaneous concentration distributions C at statistically steady state (the 15 millionth time step) for homogeneous and structurally heterogeneous porous media with $Ra_D = 5.7 \times 10^2$; (b) $\bar{\chi}$ distributions for the homogeneous and structurally heterogeneous porous media with $Ra_D = 5.7 \times 10^2$; (c) the diagram of the probability density distributions of $\bar{\chi}$ for the cases with $Ra_D = 5.7 \times 10^2$; (d) the boundary dissipation distributions at each horizontal location $\bar{\chi}_{NB}$ for the cases with $Ra_D = 5.7 \times 10^2$; (e) the instantaneous concentration distributions C at statistically steady state (the final time step) for homogeneous and structurally heterogeneous porous media with $Ra_D = 3.1 \times 10^4$; (f) $\bar{\chi}$ distributions for the homogeneous and structurally heterogeneous porous media with $Ra_D = 3.1 \times 10^4$; (g) the diagram of the probability density distributions of $\bar{\chi}$ for the cases with $Ra_D = 3.1 \times 10^4$; (h) the boundary dissipation distributions at each horizontal location $\bar{\chi}_{NB}$ for the cases with $Ra_D = 3.1 \times 10^4$.

to consider whether this well-organized pattern affects the solute transfer rates across the domain boundaries. To investigate that, the time average of normalized concentration dissipation $\overline{\chi} = \frac{\overline{D|\nabla C|^2}}{D(\Delta C)^2/H^2} = \overline{|\nabla C|^2}H^2$ (quantifying the ratio of the concentration dissipation for a R-D convection to that for a diffusion process) for time steps at statistically steady state is adopted. This is because solute transfer rates rely on pure diffusion at the boundaries, which is not straightforward. This is also reasonable as $F_{X=0}$ and χ are comparable after R-D convection reaches statistically steady state. Following GL theory (Grossmann and Lohse, 2000), we decompose the global dissipation into contributions from the bulk and boundary-layer regions in the subsequent analysis.

Here, the cases with the lowest Ra_D (5.7×10^2, *Sh* in the structurally heterogeneous porous medium is larger than that in the homogeneous medium) and the highest Ra_D (3.1×10^4, *Sh* in the structurally heterogeneous porous medium is smaller than that in the homogeneous medium) are taken as examples for analysis. It should be noted that the following analysis is expected to be applicable to cases S21–S23, as it is independent of the flow direction in the R-D convection. Due to the specific structural configuration of these cases (S21-S23), the influence of the preferential pathway on the solute transfer rate is likely insignificant.

For the cases with the lowest Ra_D, the typical instantaneous concentration distributions C at statistically steady state (the 15 millionth time step) for homogeneous and heterogeneous media illustrate two different patterns as shown in Fig. 4**(a)**. The pattern in the homogeneous medium is characterized by system-scale perturbed convection rolls, while in the heterogeneous medium it takes the form of relatively small-scale columnar flow. The observed difference in patterns is a direct result from the regulation effect of the dominant channel. Within this finite computational domain, the small-scale columnar pattern gives rise to an increased number of vertically migrating plume pairs. Thus, more dissipation hotspots are expected to occur in the heterogeneous medium.

This expectation is confirmed by the relative magnitude of the volume-averaged $\overline{\chi}$, which is 11.8 for the homogeneous medium and 14.9 for the heterogeneous medium. The two values are slightly larger than *Sh* that are 8.5 and 11.0. This may be because of numerical error. Moreover, the $\overline{\chi}$ distributions not only capture the patterns of perturbed convection rolls and columnar flow, but also qualitatively display higher bulk concentration dissipation in the heterogeneous medium, as observed in Fig. 4**(b)**. This quantitative evidence is demonstrated by the relative positions of the two distinct peaks for the homogeneous and heterogeneous media in Fig. 4 **(c)**, which proves the higher concentration dissipation in the bulk region of the heterogeneous medium. To better visualize the dissipations near the boundary, the average dissipations within boundaries at each horizontal location $\overline{\chi}_{NB}$ are plotted in Fig. 4**(d)**. Here, the thickness of boundary layer is estimated by $\lambda = \frac{1}{2}HSh^{-1}$ (Grossmann and Lohse, 2000), which is 24 and 18 for homogenous and heterogeneous media, respectively. Fig. 4**(d)** reveals distinct boundary dissipation distributions of the structurally heterogeneous medium compared to the homogeneous medium. Specifically, concentration dissipation is higher within the dominant channel but lower in other areas. In contrast, the homogeneous medium exhibits a relatively periodic and stable distribution. The different boundary dissipation distributions between homogeneous and heterogeneous media also arise from the regulation effect of the high-permeability channel.

As the Ra_D increases from 5.7×10^2 to 3.1×10^4, the flow in the homogeneous medium transitions from a convection rolls regime to a chaotic regime (Otero et al., 2004). In this chaotic regime, the R-D convection lacks large-scale circulation. Moreover, it features persistent shedding and vertical drifting of small-scale plumes, which originate from the boundaries at quasi-uniform horizontal intervals. However, in the structurally heterogeneous medium, the transport pattern is regulated by the high-permeability pathway, resulting in a dominant large-scale circulation. Driven by this large-scale circulation, the shedding of small-scale plumes becomes location-dependent. Denser plumes detach mostly near the dominant channel, whereas lighter ones break off mainly from the lateral regions. The aforementioned distinguishing features between the homogeneous and heterogeneous media are evident in concentration distributions at the final time step (Fig. 4**(e)**). Compared with the homogeneous medium, the heterogeneous medium develops fewer contacts between denser and lighter plumes, resulting in fewer dissipation hotspots. This is also proven by the volume-averaged $\overline{\chi}$, which are 65.9 and 61.1 for homogeneous and heterogeneous porous media, respectively.

The $\overline{\chi}$ distributions in Fig. 4**(f)** show the extensive low-dissipation areas in bulk of the heterogeneous medium, and the relative positions of the leftmost peaks in Fig. 4**(g)** also evidence that. For the boundary dissipation distributions, Fig. 4**(h)** clearly shows that, in contrast to the periodic and stable dissipation distribution in the homogeneous medium, concentration dissipations are enhanced within the dominant channel and confined to lower levels elsewhere. This is similar to the phenomenon in Fig. 4**(d)**, and is induced by the regulation effect of the preferential pathway. It should be noted that, here $\lambda = 3$ and $\lambda = 4$ are for homogeneous and heterogeneous media, respectively. However, these values are much smaller than the pore size. To resolve dissipation characteristics over a region spanning at least one pore size near the boundary, here the averaging window at each horizontal location encompasses 19 lattices (that is $\Delta w + \frac{N}{2}$) in the vertical direction.

For the finite computational domains, the presence of the dominant channel enhances the solute transfer rate when $Ra_D < 1.3 \times 10^3$, whereas it suppresses the rate when $Ra_D > 1.0 \times 10^4$. These contrasting behaviors result from the regulation effect of the preferential pathway on the transport pattern in R-D convection at statistically steady state. For $Ra_D < 1.3 \times 10^3$, this effect transforms the large-scale convection rolls into smaller-scale columnar flow, thereby increasing *Sh*. In contrast, for $Ra_D > 1.0 \times 10^4$, it establishes a dominant large-scale circulation, which suppresses the contacts of small-scale denser and lighter plumes, and therefore reduces *Sh*.

5. Temporal fluctuation

Given that the high-permeability pathway regulates the transport pattern in R-D convection at statistically steady state, it is reasonable to expect that the flow exhibits lower stochasticity in the structurally heterogeneous porous medium than in the homogeneous medium. To quantitively investigate that, the concentration square deviation $E_c(t) = \int\int [C(x,y,t) - \overline{C}(x,y)]^2 dxdy$ is defined to measure the magnitude of the instantaneous concentration field away from the average concentration field of all time steps at statistically steady state. We calculated the $E_c(t)$ for both heterogeneous (S1–S8) and homogeneous media (S9–S16) across various Ra_D.

Taking the cases with $Ra_D = 3.1 \times 10^4$ as examples, we plot the evolution of $E_c(t)$ for both heterogeneous and homogeneous media with time steps as shown in Fig. 5**(a)**. The results show that the E_c values in both cases are high initially, then gradually decrease, and finally oscillate, which reflects the processes of R-D convections from the initial time to the statistically steady state. We then calculated the time-averaged $E_c(t)$ for time steps at the statistically steady state, denoted as $\overline{E}_c$. It is plotted in Fig. 5**(b)**, where the error bars span from the minimum to the maximum E_c value across the averaging period.

Fig. 5**(b)** shows that the $\overline{E}_c$ values in the heterogeneous medium are lower than that in the homogeneous medium when $Ra_D < 1.3 \times 10^3$ and $Ra_D > 7.0 \times 10^3$, which means the regulation effect of the high-permeability channel on the transport pattern decreases the flow stochasticity. Especially for the cases with $Ra_D < 1.3 \times 10^3$, the $\overline{E}_c$ values are almost zero in the heterogeneous medium, which implies that the regulation effect almost erases the temporal fluctuation. However, when $1.3 \times 10^3 < Ra_D < 7.0 \times 10^3$, the flow stochasticity in the heterogeneous medium is larger although the regulation effect still exists. We speculate that this observation may be related to the flow regime transition in R-D convection, and will investigate it in the future.

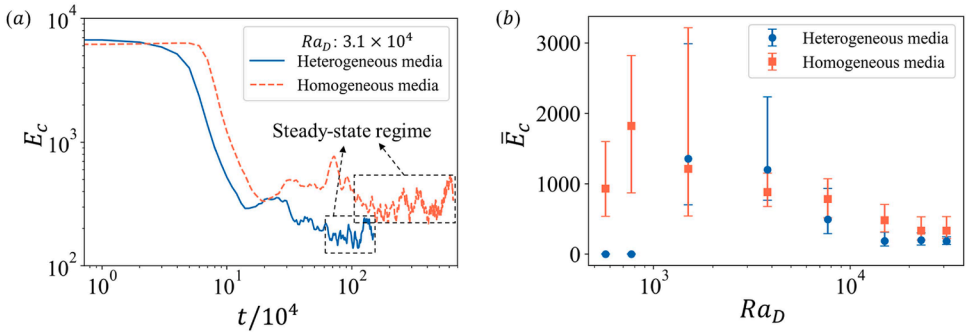


Fig. 5. (a) the evolution of the concentration square deviation E_c for the cases with $Ra_D = 3.1 \times 10^4$; (b) the $\overline{E}_c$ values for both structurally heterogeneous media (S1 ~ S8) and homogeneous media (S9 ~ S16) with the error bars spanning the range from the minimum to the maximum value of E_c across the averaging period.

In summary, the analysis of temporal fluctuation indicates that:

1) small heterogeneity leads to the great reduction of flow uncertainty in R-D convection at statistically steady state when $Ra_D < 1.3 \times 10^3$, which may be helpful for flow control;
2) the flow stochasticity in the heterogeneous medium is not necessarily lower than that in the homogeneous medium, which depends on Ra_D.

6. Conclusions

In this study, the solute transport patterns and transfer rates during statistically steady-state R-D convection in porous media with a single vertical high-permeability channel are investigated based on Lattice Boltzmann Modeling. We observe strong regulation of transport patterns by the preferential pathway. A theoretical model elucidates that transport patterns are determined by the minimization of total gravitational potential energy under the studied condition. Moreover, transport patterns are prov en to be independent of Ra_D (flow regime) and are only determined by the porous structure of the structurally heterogeneous media. The derived theor etical criterion accurately predicts the patterns obtained from simulations.

Although the regulation effect of the dominant channel on transport patterns remains consistent across different Ra_D, its impact on transfer rates and flow stochasticity varies with Ra_D. When $Ra_D < 1.3 \times 10^3$, the solute transfer rate in structurally heterogeneous media exceeds that in homogeneous media. As Ra_D increases, the solute transfer rates in both media become comparable, and for $Ra_D > 1 \times 10^4$, the homogenous media system exhibits a higher transfer rate. This behavior results from the preferential pathway promoting a columnar flow pattern at lower Ra_D ($Ra_D < 1.3 \times 10^3$), whereas it inducing a large-scale circulation at higher Ra_D ($Ra_D > 1 \times 10^4$). Furthermore, the regulation role of the high-permeability channel is shown to suppress flow stochasticity when $Ra_D < 1.3 \times 10^3$ and $Ra_D > 7.0 \times 10^3$.

This paper presents systematic investigation of structural heterogeneity effects on solute transport patterns and transfer rates in statistically steady-state R-D convection, together with the underlying physical mechanisms. The findings offer theoretical insights relevant to subsurface hydrological engineering such as CO_2 sequestration.

7. Limitations

Constrained by limitations of Lattice Boltzmann Model and by computational demands, a detailed investigation of two potentially influential parameters for R-D convections at statistically steady state is reserved for future studies. The first involves the aspect ratio of the computational domain. We expect the regulation effect of the high-permeability pathway to be limited, with its extent possibly controlled by the width of preferential channel. Therefore, for large aspect ratios, this effect may be insufficient to fully affect convection within the surrounding porous medium, particularly in the far-field regions distant from the dominant channel. Thus, the convective transport dynamic may be different under the condition of large aspect ratio. This also suggests that further upscaling works remain necessary to extend the present (locally valid) conclusions to larger scales, even though pore-scale simulations in this study already reach the centimeter scale.

The second refers to the ratio of the pore size in the surrounding porous medium to the boundary-layer thickness in R-D convections. The simulation cases in this work mainly focus on ratios around or much larger than 1. Cases with ratios significantly smaller than 1 need be further investigated as the solute transport kinetics is different (Schwendener et al., 2026). Thus, it may affect the present analysis.

Nevertheless, this study reveals the important phenomena and the underlying mechanisms of R-D convections at statistically steady state in structurally heterogeneous porous media, which provides a solid foundation for future investigations. Extending present analysis to above two aspects and more complex heterogeneous systems constitutes an important next step. Finally, we recognize that geological CO_2 sequestration primarily involves the one-sided R-D convection (De Paoli, 2023). Nonetheless, the present statistically steady-state analysis may still be applicable to the shutdown stage of convective CO_2 transport. This is because the dynamical structure of one-sided flow in the shutdown regime is qualitatively similar to upper half of a RB-type (i.e., two-sided) cell, and its transport kinetics during shutdown regime can be quantitatively described by the RB-type Sh-Ra_D scaling (Hewitt et al., 2013).

CRediT authorship contribution statement

Jingwei Zhu: Writing – original draft, Visualization, Software, Investigation, Formal analysis. **Jingsen Feng:** Software. **Chiyu Xie:** Supervision. **Hang Deng:** Writing – review & editing, Supervision, Resources. **Jianing Yang:** Data curation. **Yumin Wang:** Software. **Ke Xu:** Writing – review & editing, Supervision, Investigation, Funding acquisition, Conceptualization.

Declaration of competing interest

The authors declare that they have no known competing financial interests or personal relationships that could have appeared to influence the work reported in this paper.

Acknowledgement

We gratefully acknowledge the financial support and funding provided by the National Key R&D Program of China (Grant No. 2021YFB1507405), Fundamental and Interdisciplinary Disciplines Breakthrough Plan of the Ministry of Education of China (JYB2025XDXM301), the National Natural Science Foundation of China (No. U23B6004), and the China National Petroleum Corporation-Peking University Strategic Cooperation Project of Fundamental Research. We declare no conflict of interest.

Appendix A. On the insensitivity to initial conditions

Without loss of generality, three cases that employ S17-type computational domain (detailed parameters shown in Table 1) are simulated to verify the effect of initial conditions on the solute transport pattern and solute transfer rate in R-D convection at statistically steady state. Three simulations are identical in any other respects except initial conditions. As the established theoretical model predicts that denser fluid migrates downward through the preferential pathway while lighter fluid ascends through the surrounding porous medium at statistically steady state in this type of the structurally heterogeneous porous medium, the following inverted initial configurations are defined, respectively: (1) Simulation A1 imposing an upward velocity in the dominant channel against a downward velocity in the surrounding porous medium (initial velocity being $u = \frac{k_{vet} g \beta \Delta C}{\nu}$), while maintaining a vertically linear solute distribution, (2) Simulation A2 placing lighter fluid ($C = 0$) in the dominant channel and denser fluid ($C = 1$) in the surrounding porous medium and starting from a state of zero velocity field, and (3) Simulation A3 combining the contrasting features of the previous two, and assigning upward velocity with lighter fluid to the dominant channel and downward velocity with denser fluid to the surrounding porous medium.

Fig. A**(a)** shows the average streamline of all time at statistically steady state of Simulation A3, which demonstrates that the fluids descend in the high-permeability pathway while generally ascend in the surrounding porous medium. Similar behaviors are observed in Simulations A1 and A2. As denser fluids stand in the top boundary and lighter fluids sit at the bottom boundary, it is reasonable to expect the denser fluids go downward through the dominant pathway while lighter fluids go upward through the surrounding porous medium. To evidence that, the net vertical solute flux $F_s = \int \int u_x c dx dy$ in the dominant channel and the surrounding porous medium, respectively, are calculated, as shown in Fig. A**(b)**. The results show that at the later stage, the F_s in the dominant channel is always larger than 0, however, F_s in the surrounding porous medium is smaller than 0, which confirms a common transport pattern across all three simulations, consistent with the theoretical prediction upon reaching statistically steady state. It should be noted that F_s in the dominant channel and the surrounding porous medium for each case are not symmetric. This is because the lattice concentration range $C \in [0, 1]$ is not symmetric about 0. Therefore, the initial conditions have no influence on the transport pattern in R-D convection at statistically steady state.

For the solute transfer rate, the average *Sh* values for the three simulations after the systems reach statistically steady state are 42.28, 42.74, and 42.86, respectively. Given the minimal variation among the three values, the results prove that the impact of initial conditions on the solute transfer rate is negligible.

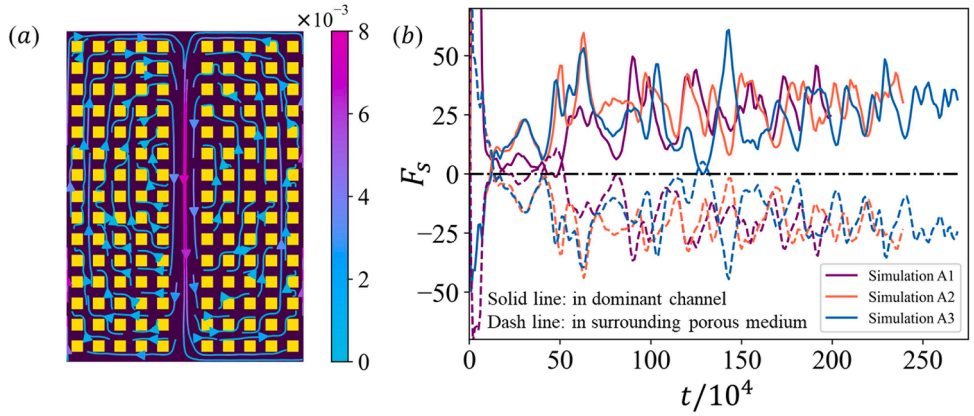


Fig. A. (a) the average streamline of all time at statistically steady state of Simulation A3; (b) vertical solute flux for Simulation A1, A2, and A5 at different time.

Appendix B. Permeability calculation in porous media using LBM

We apply LBM to calculate the effective vertical permeability of structurally heterogeneous porous media (k^*_{vet}), along with the respective vertical permeabilities of their constituent preferential channels (k^*_{ch}) and surrounding porous media (k^*_m). Here, the LBM is restricted to solving the continuity equation (Eq. (2)) and the Navier–Stokes equation without coupling solute transport

$$\frac{\partial \vec{u}^*}{\partial t^*} + \vec{u}^* \cdot \vec{\nabla} \vec{u}^* = \frac{1}{\rho^*} \vec{\nabla} p^* + \nu^* \nabla^2 \vec{u}^* + \vec{g}^* \tag{B1}$$

Therefore, this can be solved only using a single distribution LBGK model, as expressed in Eq. (5). It should be noted that the force term in Eq. (5) is modified to $F_i = \left(1 - \frac{\Delta t}{2\tau_f}\right) \frac{f_i^{eq}}{\rho} \frac{\vec{e}_i - \vec{u}}{c_s^2} \cdot \rho_{ref} \vec{g}$ as the solute effect vanishes.

Fig. B**(a)** illustrates boundary conditions for calculating vertical permeability of structurally heterogeneous porous media. Driven by gravity, fluid continuously enters the domain through the top boundary and exits through the bottom boundary. Once the flow attains a statistically steady state, the vertical permeability of the medium is evaluated using Darcy's law

$$k^*_{vet} = \frac{\nu^* [\![u^*]\!]}{g^*} \tag{B2}$$

where $[\![\cdot]\!]$ denotes the average over the whole computational domain. The above procedure and boundary settings are also applied to calculate the vertical permeability of homogeneous\surrounding porous media. For calculating the vertical permeability of the dominant channel, we apply the no-slip condition to the lateral boundaries as shown in Fig. B**(b)**. This is because the fluid in the channel experiences shear friction mainly from lateral sides. The computational procedure for the dominant channel is the same as described above.

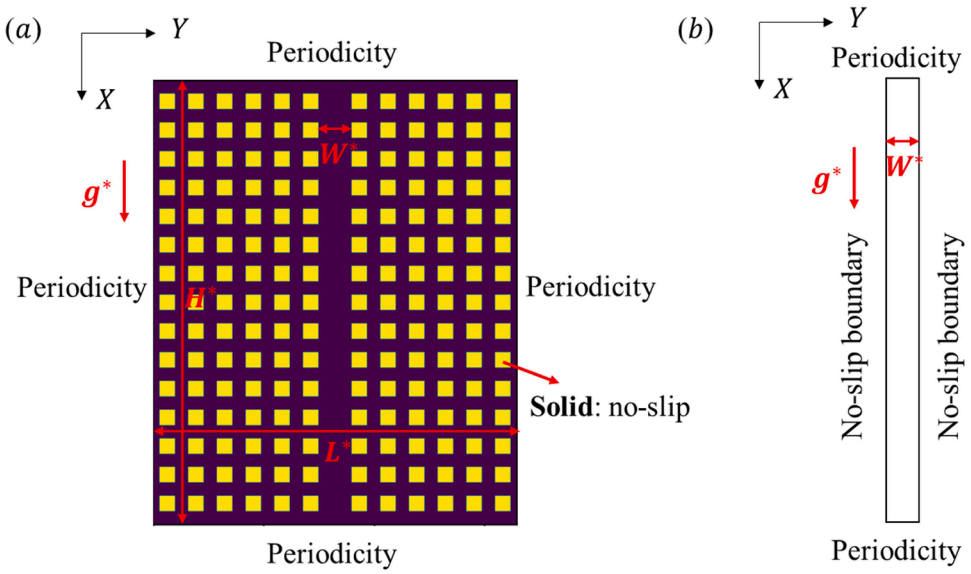


Fig. B. (a) the boundary conditions for calculating the vertical permeability of structurally heterogeneous and homogeneous porous media; (b) the boundary conditions for calculating the vertical permeability of the dominant channel.

Appendix C. Summary of assumptions

Table C
Summary of assumptions used in this study.

Category	No.	Assumption
Numerical model		
	1	Fluid density depends linearly on concentration
	2	The Boussinesq approximation is valid
	3	The flow is incompressible
	4	Fluid viscosity is independent of concentration
	5	The solid particles are rigid
Theoretical model		
	1	Possible transitional zones are negligible
	2	The flow within the preferential channel is unidirectional
	3	The Boussinesq approximation is valid
	4	Fluid density is uniform within subdomains 1 and 2, respectively
	5	Fluid viscosity is independent of concentration
	6	The solid particles are rigid

Appendix D. Unit conversion

The physical unit (with superscript *) of physical quantities are linked to the lattice unit (without superscript *) through conversion coefficients. By setting three conversion coefficients, $C_v = \frac{v^*}{v} = 3.1 \times 10^{-6}\ m^2/s$, $C_\rho = \frac{\rho^*}{\rho} = 10^3\ kg/m^3$, and $C_{xy} = \frac{\Delta x^*}{\Delta x} = \frac{\Delta y^*}{\Delta y} = 25\ \mu m$ (with $v = \frac{1}{3.1}$, $\rho_{ref} = 1$, and $\Delta x = \Delta y = 1$), the conversion coefficient of rest parameters can be conducted as $C_u = \frac{C_v}{C_{xy}} = 0.124\ m/s$, $C_t = \frac{C_{xy}^2}{C_v} = 2 \times 10^{-4}\ s$, $C_p = \frac{C_\rho C_v^2}{C_{xy}^2} = 15.376\ Pa$, $C_g = \frac{C_v^2}{C_{xy}^3} = 615.04\ m/s^2$, and $C_k = C_{xy}^2 = 6.25 \times 10^{-10}\ m^2$. Therefore, physical quantities can be converted to lattice unit based on these conversion coefficients.

Appendix E. Model validation

The established LBM is validated through three benchmark problems, Hagen-Poiseuille flow, heat diffusion in a plate (Mohamad, 2019), and Rayleigh–Bénard convection as shown in Fig. E. For the Hagen-Poiseuille flow, the velocity profile at statistically steady state is calculated and the simulation result is compared with theoretical result, which shows good agreement. For heat diffusion in a plate, the temperature at the center of the horizontal domain under the statistically steady-state condition is measured and compared with the result from Mohamad (2019). This comparison demonstrates good agreement between the simulations. For the Rayleigh–Bénard convection, the *Sh* values at various Rayleigh numbers are computed in statistically steady state and compared with the results of He et al., (2009), Clever & Busse (1974), and Fromm (1965). The results show that our results compare favorably with prior work. Therefore, the established LBM is full validated.

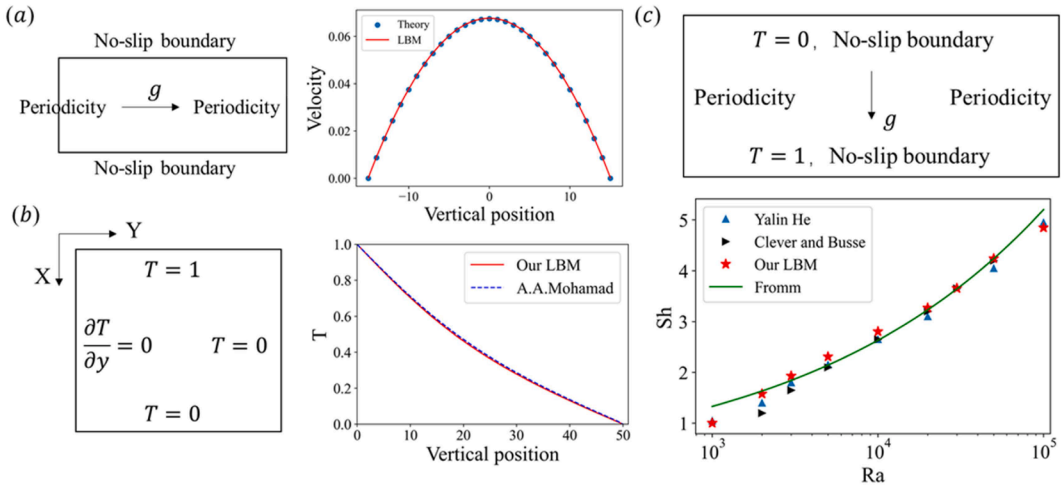


Fig. E. (a) problem setup of Hagen-Poiseuille flow and the comparison results; (b) problem setup of heat diffusion in a plate and the comparison results; (c) problem setup of Rayleigh–Bénard convection and the comparison results.

Appendix F. Comparisons of the total gravitational potential energy and the total kinetic energy

The total gravitational potential energy and the total kinetic energy for the cases S8, S18, S20, and S23 are compared, as these have the highest Ra_D values (detailed values are shown in Table 1) for each distinct configuration of structurally heterogeneous porous media. Fig. F shows that for all cases, the total gravitational potential energy is always much larger than the total kinetic energy. Therefore, the total kinetic energy can be neglected compared with the total gravitational potential energy.

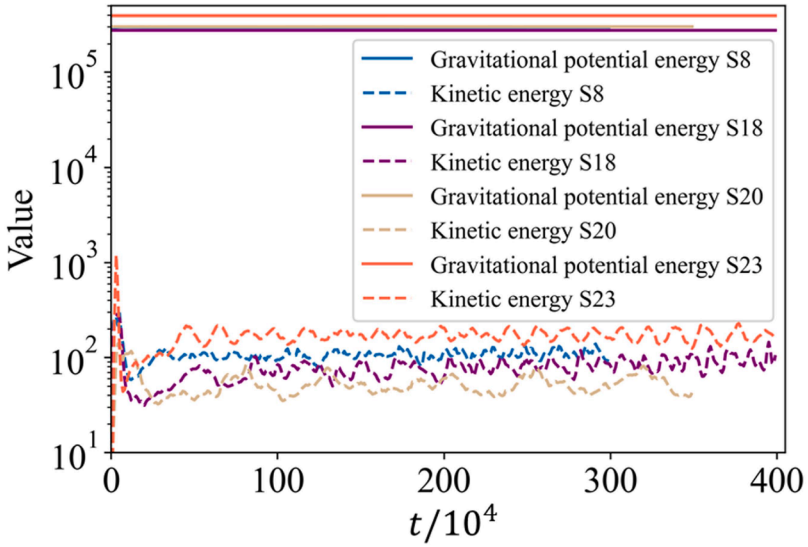


Fig. F. Comparisons of the total gravitational potential energy and the total kinetic energy for the cases S8, S18, S20, and S23 at different time.

Data availability

Data will be made available on request.

References

Anderson, D.M., Guba, P., 2020. Convective phenomena in mushy layers. Annu Rev. Fluid. Mech. 52 (1), 93–119. https://doi.org/10.1146/annurev-fluid-010719-060332.

Benhammadi, R., Hidalgo, J.J., 2025. Impact of porous media heterogeneity on convective mixing in a Rayleigh–Bénard instability. Adv. Water. Resour. 206, 105139. https://doi.org/10.1016/j.advwatres.2025.105139.

Bond, C.E., Kremer, Y., Johnson, G., Hicks, N., Lister, R., Jones, D.G., Pearce, J., 2017. The physical characteristics of a CO2 seeping fault: the implications of fracture permeability for carbon capture and storage integrity. Int. J. Greenh. Gas Control 61, 49–60. https://doi.org/10.1016/j.ijggc.2017.03.020.

Chen, S., Doolen, G.D., 1998. Lattice Boltzmann method for fluid flows. Annu Rev. Fluid. Mech. 30 (1), 329–364. https://doi.org/10.1146/annurev.fluid.30.1.329.

Chen, C., Zhang, D., 2010. Pore-scale simulation of density-driven convection in fractured porous media during geological CO 2 sequestration. Water. Resour. Res. 46 (11), 2010WR009453. https://doi.org/10.1029/2010WR009453.

Clever, R.M., Busse, F.H., 1974. Transition to time-dependent convection. J. Fluid. Mech. 65 (4), 625–645. https://doi.org/10.1017/S0022112074001571.

Day, P.W., 1972. Rearrangement inequalities. Can. J. Math. 24 (5), 930–943. https://doi.org/10.4153/CJM-1972-093-x.

De Paoli, M., Zonta, F., Soldati, A., 2016. Influence of anisotropic permeability on convection in porous media: implications for geological CO2 sequestration. Phys. Fluids 28 (5), 056601. https://doi.org/10.1063/1.4947425.

De Paoli, M., Alipour, M., Soldati, A., 2020. How non-Darcy effects influence scaling laws in Hele-Shaw convection experiments. J. Fluid. Mech. 892, A41. https://doi.org/10.1017/jfm.2020.229.

De Paoli, M., Pirozzoli, S., Zonta, F., Soldati, A., 2022. Strong Rayleigh–Darcy convection regime in three-dimensional porous media. J. Fluid. Mech. 943, A51. https://doi.org/10.1017/jfm.2022.461.

De Paoli, M., 2023. Convective mixing in porous media: a review of Darcy, pore-scale and Hele-Shaw studies. Eur. Phys. J. E 46 (12), 129. https://doi.org/10.1140/epje/s10189-023-00390-8.
Dutta, R., Singh, R., Chakraborty, R., Kundu, G., Mandal, A., 2025. Optimisation of CO2 storage in saline aquifers: a field-scale mechanistic study on injection strategies, pressure management, and long-term containment. Environ. Earth. Sci. 84 (13), 388. https://doi.org/10.1007/s12665-025-12390-2.
Fromm, J.E., 1965. Numerical solutions of the nonlinear equations for a heated fluid layer. Phys. Fluids 8 (10), 1757–1769. https://doi.org/10.1063/1.1761107.
Graf, T., Therrien, R., 2005. Variable-density groundwater flow and solute transport in porous media containing nonuniform discrete fractures. Adv. Water. Resour. 28 (12), 1351–1367. https://doi.org/10.1016/j.advwatres.2005.04.011.
Grossmann, S., Lohse, D., 2000. Scaling in thermal convection: a unifying theory. J. Fluid. Mech. 407, 27–56. https://doi.org/10.1017/S0022112099007545.
Grossmann, S., Lohse, D., 2001. Thermal convection for large Prandtl numbers. Phys. Rev. Lett. 86 (15), 3316–3319. https://doi.org/10.1103/PhysRevLett.86.3316.
Han, L., Shi, X., Ni, H., Zhang, W., Gao, Q., 2024. Review of CO2 fracturing and carbon storage in shale reservoirs. Energy Fuels. 38 (17), 15913–15934. https://doi.org/10.1021/acs.energyfuels.4c02353.
He, Y., Li, Q., Wang, Y., Tang, G., 2009. Lattice Boltzmann method and its applications in engineering thermophysics. Chin. Sci. Bull. 54 (22), 4117–4134.
He, X., Shan, X., Doolen, G.D., 1998. Discrete Boltzmann equation model for nonideal gases. Phys. Rev. E 57 (1), R13–R16. https://doi.org/10.1103/PhysRevE.57.R13.
Hewitt, D.R., Neufeld, J.A., Lister, J.R., 2013. Convective shutdown in a porous medium at high Rayleigh number. J. Fluid. Mech. 719, 551–586. https://doi.org/10.1017/jfm.2013.23.
Hewitt, D.R., 2020. Vigorous convection in porous media. Proc. R. Soc. A: Math. Phys. Eng. Sci. 476 (2239), 20200111. https://doi.org/10.1098/rspa.2020.0111.
Hidalgo, J.J., Carrera, J., 2009. Effect of dispersion on the onset of convection during CO_2 sequestration. J. Fluid. Mech. 640, 441–452. https://doi.org/10.1017/S0022112009991480.
Hidalgo, J.J., Fe, J., Cueto-Felgueroso, L., Juanes, R., 2012. Scaling of convective mixing in porous Media. Phys. Rev. Lett. 109 (26), 264503. https://doi.org/10.1103/PhysRevLett.109.264503.
Horton, C.W., Rogers, F.T., 1945. Convection currents in a porous medium. J. Appl. Phys. 16 (6), 367–370. https://doi.org/10.1063/1.1707601.
Hosseini, N., Bajalan, Z., Khoei, A.R., 2020. Numerical modeling of density-driven solute transport in fractured porous media with the extended finite element method. Adv. Water. Resour. 136, 103453. https://doi.org/10.1016/j.advwatres.2019.103453.
Hu, C., Xu, K., Yang, Y., 2023. Effects of the geothermal gradient on the convective dissolution in CO_2 sequestration. J. Fluid. Mech. 963, A23. https://doi.org/10.1017/jfm.2023.349.
Huppert, H.E., Neufeld, J.A., 2014. The fluid mechanics of carbon dioxide sequestration. Annu Rev. Fluid. Mech. 46 (1), 255–272. https://doi.org/10.1146/annurev-fluid-011212-140627.
Iding, M., Blunt, M.J., 2011. Enhanced solubility trapping of CO2 in fractured reservoirs. Energy Procedia 4, 4961–4968. https://doi.org/10.1016/j.egypro.2011.02.466.
Iding, M., Ringrose, P., 2010. Evaluating the impact of fractures on the performance of the In Salah CO2 storage site. Int. J. Greenh. Gas Control 4 (2), 242–248. https://doi.org/10.1016/j.ijggc.2009.10.016.
Ju, L., Shan, B., Guo, Z., 2022. Pore-scale study of convective mixing process in brine sequestration of impure CO 2. Phys. Rev. Fluids. 7 (11), 114501. https://doi.org/10.1103/PhysRevFluids.7.114501.
Kaydani, H., Mohebbi, A., 2017. Experimental and numerical study of the onset of transient natural convection in a fractured porous medium. Transp. Porous. Media 116 (2), 923–939. https://doi.org/10.1007/s11242-016-0806-8.
Kim, M., Kim, K., Han, W.S., Oh, J., Park, E., 2019. Density-driven convection in a fractured porous Media: implications for geological CO $_2$ storage. Water. Resour. Res. 55 (7), 5852–5870. https://doi.org/10.1029/2019WR024822.
Krüger, T., Kusumaatmaja, H., Kuzmin, A., Shardt, O., Silva, G., Viggen, E.M., 2017. The Lattice Boltzmann Method: Principles and Practice. Springer International Publishing, Cham. https://doi.org/10.1007/978-3-319-44649-3.
Landman, A.J., Johannsen, K., Schotting, R., 2007. Density-dependent dispersion in heterogeneous porous media part I: a numerical study. Adv. Water. Resour. 30 (12), 2467–2480. https://doi.org/10.1016/j.advwatres.2007.05.016.
Lasser, J., Nield, J.M., Ernst, M., Karius, V., Wiggs, G.F.S., Threadgold, M.R., et al., 2023. Salt polygons and porous Media convection. Phys. Rev. X. 13 (1), 011025. https://doi.org/10.1103/PhysRevX.13.011025.
Letelier, J.A., Mujica, N., Ortega, J.H., 2019. Perturbative corrections for the scaling of heat transport in a Hele-Shaw geometry and its application to geological vertical fractures. J. Fluid. Mech. 864, 746–767. https://doi.org/10.1017/jfm.2019.3.
Li, Q., Cai, W.H., Li, B.X., Chen, C.-Y., 2020. Numerical study of density-driven convection in laminated heterogeneous porous Media. J. Mech. 36 (5), 665–673. https://doi.org/10.1017/jmech.2020.32.
Li, J., Yang, Y., Sun, C., 2025. From Darcy convection to free-fluid convection: pore-scale study of density-driven currents in porous media. J. Fluid. Mech. 1009, A10. https://doi.org/10.1017/jfm.2025.213.
Liu, B., Yao, J., 2023. Numerical study on density-driven convection of CO2-H2S mixture in fractured and sequential saline aquifers. Front. Energy Res. 11, 1241672. https://doi.org/10.3389/fenrg.2023.1241672.
Liyanage, R., Fu, X., Pini, R., Juanes, R., 2024. Direct comparison of density-driven convective mixing in a three-dimensional porous medium using experiments and simulation. Phys. Rev. Fluids. 9 (4), 043802. https://doi.org/10.1103/PhysRevFluids.9.043802.
Mezon, C., Mourzenko, V.V., Thovert, J.-F., Antoine, R., Fontaine, F., Finizola, A., Adler, P.M., 2018. Thermal convection in three-dimensional fractured porous media. Phys. Rev. E 97 (1), 013106. https://doi.org/10.1103/PhysRevE.97.013106.
Mohamad, A.A., 2019. Lattice Boltzmann Method: Fundamentals and Engineering Applications with Computer Codes. Springer London, London. https://doi.org/10.1007/978-1-4471-7423-3.
Murphy, H.D., 1979. Convective instabilities in vertical fractures and faults. J. Geophys. Res.: Solid Earth 84 (B11), 6121–6130. https://doi.org/10.1029/JB084iB11p06121.
Nick, H.M., Schotting, R., Gutierrez-Neri, M., Johannsen, K., 2009. Modeling transverse dispersion and variable density flow in porous Media. Transp. Porous. Media 78 (1), 11–35. https://doi.org/10.1007/s11242-008-9277-x.
Otero, J., Dontcheva, L.A., Johnston, H., Worthing, R.A., Kurganov, A., Petrova, G., Doering, C.R., 2004. High-Rayleigh-number convection in a fluid-saturated porous layer. J. Fluid. Mech. 500, 263–281. https://doi.org/10.1017/S0022112003007298.
Parisio, F., Vilarrasa, V., Wang, W., Kolditz, O., Nagel, T., 2019. The risks of long-term re-injection in supercritical geothermal systems. Nat. Commun. 10 (1), 4391. https://doi.org/10.1038/s41467-019-12146-0.
Peters, E.J., 2012. Advanced petrophysics, 1st ed. Live Oak Book Company, Austin, TX.
Sabet, N., Hassanzadeh, H., De Wit, A., Abedi, J., 2021. Scalings of Rayleigh-Taylor instability at large viscosity contrasts in porous Media. Phys. Rev. Lett. 126 (9), 094501. https://doi.org/10.1103/PhysRevLett.126.094501.
Santos, E., Javier, Y., Ying, P., Masa, G., Alex, L., Nicholas, K., Hasan, J., 2021. 3D Collection of Binary Images. Digital Porous Media, Digital Porous Media. https://doi.org/10.17612/nxgk-k611. Accessed.
Schwendener, D.M., Noir, J., Latt, J., Coreixas, C., Kong, X.-Z., 2026. Dynamic confinement controls the porous-to-free convection transition. Proc. Natl. Acad. Sci. 123 (22), e2533675123. https://doi.org/10.1073/pnas.2533675123.
Shikaze, S.G., Sudicky, E.A., Schwartz, F.W., 1998. Density-dependent solute transport in discretely-fractured geologic media: is prediction possible? J. Contam. Hydrol. 34 (3), 273–291. https://doi.org/10.1016/S0169-7722(98)00080-1.
Slim, A.C., 2014. Solutal-convection regimes in a two-dimensional porous medium. J. Fluid. Mech. 741, 461–491. https://doi.org/10.1017/jfm.2013.673.
Sun, L., Liu, Y., Cheng, Z., Jiang, L., Lv, P., Song, Y., 2023. Review on Multiscale CO_2 mineralization and geological storage: mechanisms, characterization, modeling, applications and perspectives. Energy Fuels. 37 (19), 14512–14537. https://doi.org/10.1021/acs.energyfuels.3c01830.
Talabi, O., Ren, G., Misra, S., 2026. AI-driven rapid forecasting of CO2 plume migration and trapping efficiency in geological carbon storage. Int. J. Greenh. Gas Control 149, 104535. https://doi.org/10.1016/j.ijggc.2025.104535.
Teng, Y., Wang, P., Jiang, L., Liu, Y., Song, Y., Wei, Y., 2020. An experimental study of density-driven convection of fluid pairs with viscosity contrast in porous media. Int. J. Heat. Mass Transf. 152, 119514. https://doi.org/10.1016/j.ijheatmasstransfer.2020.119514.
Tsinober, A., Shavit, U., Rosenzweig, R., 2023. Numerical investigation of the influence of hydrodynamic dispersion on solutal natural convection. Water. Resour. Res. 59 (5), e2023WR034475. https://doi.org/10.1029/2023WR034475.
Vujević, K., Graf, T., Simmons, C.T., Werner, A.D., 2014. Impact of fracture network geometry on free convective flow patterns. Adv. Water. Resour. 71, 65–80. https://doi.org/10.1016/j.advwatres.2014.06.001.
Wang, M., Pan, N., 2008. Predictions of effective physical properties of complex multiphase materials. Mater. Sci. Eng.: R.: Rep. 63 (1), 1–30. https://doi.org/10.1016/j.mser.2008.07.001.
Wang, S., Cheng, Z., Zhang, Y., Jiang, L., Liu, Y., Song, Y., 2021. Unstable density-driven convection of CO_2 in homogeneous and heterogeneous porous Media with implications for deep saline aquifers. Water. Resour. Res. 57 (3), e2020WR028132. https://doi.org/10.1029/2020WR028132.
... & Wang, Y., Xie, J.H., Yang, W., Li, X., Abulaiti, Z., Zheng, S., Xu, K., 2025. Permafrost thawing under overlaying salt water. Sci. Adv. 11 (13), eadp2808. https://doi.org/10.1126/sciadv.adp2808.
Xu, W., Chen, R., Hu, Y., Chen, Y., Li, J., Zhuang, D., 2024. Effects of roughness on density-driven convection of dissolved CO2 in discrete fracture-matrix system. Comput. Geotech. 166, 105996. https://doi.org/10.1016/j.compgeo.2023.105996.
Xuan, Z.-H., Fang, W.-Z., Lu, Y.-H., Yang, C., Tao, W.-Q., 2024. Significance of the natural convection to the heat transfer of porous media: a pore-scale study. Int. J. Heat. Mass Transf. 222, 125163. https://doi.org/10.1016/j.ijheatmasstransfer.2023.125163.
Yang, J., Latychev, K., Edwards, R.N., 1998. Numerical computation of hydrothermal fluid circulation in fractured Earth structures. Geophys. J. Int. 135 (2), 627–649. https://doi.org/10.1046/j.1365-246X.1998.00669.x.
Zhang, Q., Xu, Q., Yang, Y., Iglauer, S., Liu, J., Liu, F., et al., 2024. Permeability heterogeneity effects on density-driven CO2 natural convection and carbon sequestration efficiency. Fuel 363, 130871. https://doi.org/10.1016/j.fuel.2024.130871.
Zhao, B., MacMinn, C.W., Huppert, H.E., Juanes, R., 2014. Capillary pinning and blunting of immiscible gravity currents in porous media. Water. Resour. Res. 50 (9), 7067–7081. https://doi.org/10.1002/2014WR015335.
Zhu, X., Fu, Y., De Paoli, M., 2024. Transport scaling in porous media convection. J. Fluid. Mech. 991, A4. https://doi.org/10.1017/jfm.2024.528.